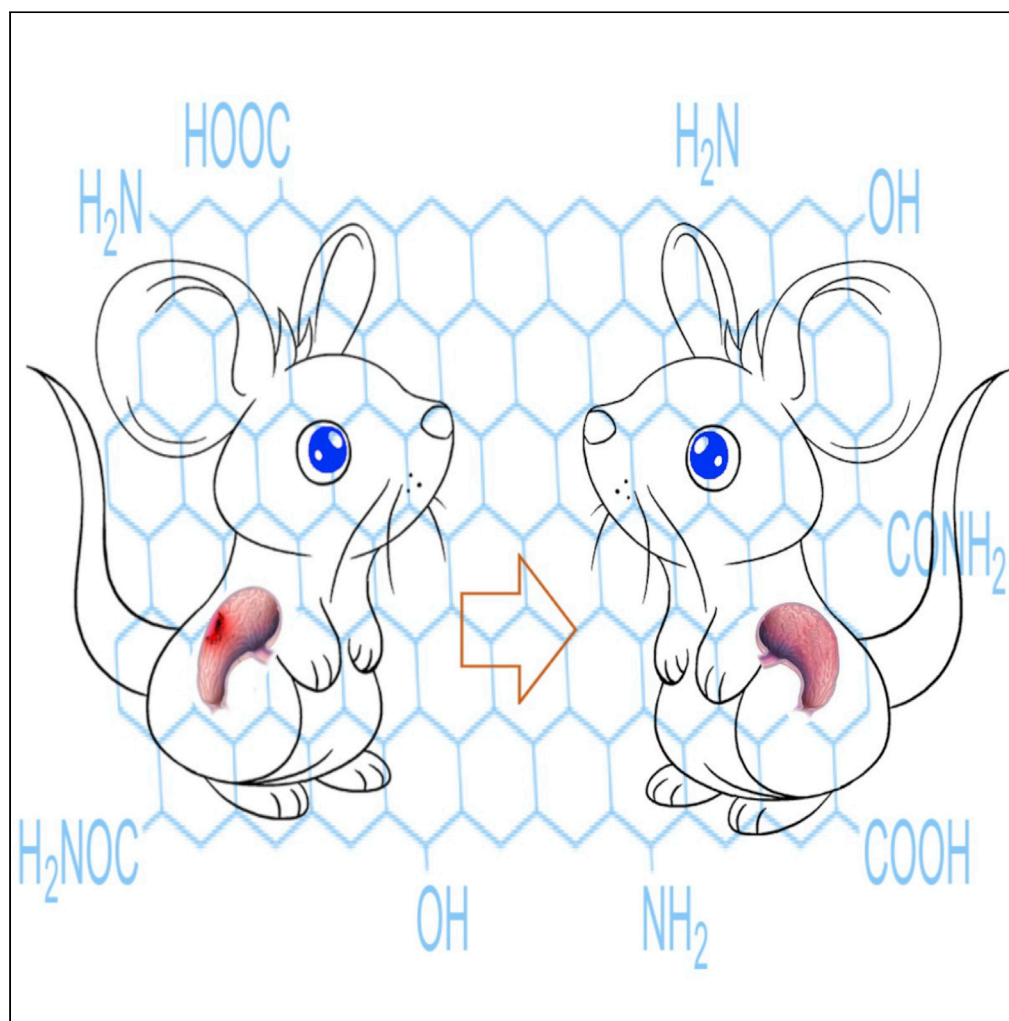


Article

Graphene quantum dots alleviate ROS-mediated gastric damage



Preeti Choudhary,
Sushama Biswas,
Noufal Kandoth,
..., Amitava Das,
Snehasikta
Swarnakar, Sumit
Kumar Pramanik

amitava@iiserkol.ac.in (A.D.)
sikta@iicb.res.in (S.S.)
samitc@goa.bits-pilani.ac.in
(S.C.)
sumitpramanik@csmcni.res.in
(S.K.P.)

Highlights

The gastrointestinal tract
is one of the major sites for
ROS generation •

Graphene quantum dots
(GQDs) have broad-
spectrum antioxidant
properties •

GQDs scavenge the ROS
and suppress gastric
ulcers by targeting the
MMP-9 pathway

Choudhary et al., iScience 25,
104062
April 15, 2022 © 2022 The
Author(s).
[https://doi.org/10.1016/
j.isci.2022.104062](https://doi.org/10.1016/j.isci.2022.104062)

Article

Graphene quantum dots alleviate ROS-mediated gastric damage

Preety Choudhary,¹ Sushama Biswas,² Noufal Kandoth,³ Deepak Tayde,^{2,4} Abhishek Chatterjee,¹ Samit Chattopadhyay,^{5,*} Amitava Das,^{3,*} Snehasikta Swarnakar,^{1,*} and Sumit Kumar Pramanik^{2,4,6,*}

SUMMARY

The gastrointestinal (GI) tract is one of the major sites for reactive oxygen species generation (ROS). Physiological ROS, lower than the threshold concentration, is beneficial for human physiology to preserve gut functional integrity. However, ROS generated in large quantities in presence of external stimuli overwhelms the cellular antioxidant defense mechanism and results in oxidative damage and associated physiological disorder. Graphene quantum dots (GQDs) are a class of carbon-based nanomaterials that have attracted tremendous attention not only for their tunable optical properties but also for their broad-spectrum antioxidant properties. In this report we have shown that GQDs are highly efficient in scavenging ROS and suppressing stress-induced gastric ulcers by targeting the MMP-9 pathway and reducing the inflammatory burden by suppressing excessive oxidative stress by inducing high caspase activity, overproduction of Bax, and downregulation of BCL2.

INTRODUCTION

The significance of keeping up physiological degrees of ROS in the gastrointestinal (GI) tract is critical for persistent intestinal inflammatory disorders. However, the specific role of the tightly regulated redox balance on multifactorial gastrointestinal inflammation generation is a subject of intense debate and is still not well understood (Aviello and Knaus, 2017). Lower ROS level due to impaired NADPH oxidase activity is linked to Crohn disease and pancolitis (Aviello and Knaus, 2017; Patlevič et al., 2016), whereas higher ROS level caused by overexpression of oxidases or mitochondrial function alteration is associated with ulcerative colitis and ileitis (Aviello and Knaus, 2018). Ulcers and ulcerative colitis are the most prevalent diseases, accounting for ~5% of the world's population (Ungaro et al., 2017). The hydroxyl or/and superoxide radicals ($\cdot\text{OH}/\cdot\text{O}_2^-$) are among the most prevalent ROS species that cause gastric ulceration and lesions. The higher level of $\cdot\text{O}_2^-$ and inactivation of superoxide dismutase are linked to the pathogenesis of Barrett esophagus and its transformation to adenocarcinoma (Bandyopadhyay et al., 1999; Bhattacharyya et al., 2014; Pérez et al., 2017; Taylor and Colgan, 2017). Certain prescription drugs are developed over the last few decades and are proven effective in controlling such disease states. However, their long-term maintenance use is not recommended because of their side effects such as swelling, headache, myalgia, nausea, weight gain, growth problems, osteoporosis, problems associated with bone marrow, etc. (Kinoshita et al., 2018; Strand et al., 2017). Such limitations imposed by the intrinsic properties of the materials employed offer a distinct scope for developing alternate efficient therapeutic agents for prolonged use for treating gastric hyperacidity and ulcers. As an elevated level of $\cdot\text{OH}/\cdot\text{O}_2^-$ accounts for these disease states, an efficient antioxidant is expected to scavenge such ROS species and inhibit the damage. Recent reports also reveal that graphene quantum dots (GQDs) exhibit radical scavenging activity, which varied with the changes in the nature of ROS species via different radical inhibition mechanisms. Graphene and GQDs have come out as important materials for various biomedical applications due to their biocompatibility, unique optical, chemical, and physicochemical properties. GQDs are a member of zero-dimensional nano-structured materials with a lateral size of less than 100 nm having a few layers of sp^2 -hybridized along with some sp^3 -hybridized carbon atoms linked to certain oxygen-containing functional groups (Zhang et al., 2012). All these allow GQDs to a delicate balance between hydrophobicity and hydrophilicity, unique dispersibility in an aqueous medium, and cell membrane permeance. Importantly, synthetic methodologies enable us to synthesize GQDs with desired reproducibility and repeatability from relatively inexpensive carbon precursors, as well as to achieve the chosen functionalization and large-scale production (Middha and Liu, 2020; Patel et al., 2019; Sandler et al., 2019; Yang et al., 2020). An earlier report also reveals that

¹CSIR-Indian Institute of Chemical Biology, 4, Raja S. C. Mullick Road, Kolkata 700 032, India

²CSIR-Central Salt and Marine Chemicals Research Institute, Bhavnagar, Gujarat, India

³Department of Chemical Sciences, Indian Institute of Science Education and Research, Kolkata 741246, India

⁴Academy of Scientific and Innovative Research (AcSIR), Ghaziabad 201002, India

⁵BITS Pilani K K Birla Goa Campus, NH 17B, Bypass, Road, Zuarinagar, Sancoale, Goa 403726, India

⁶Lead contact

*Correspondence: amitava@iiserkol.ac.in (A.D.), sikta@iicb.res.in (S.S.), samitc@goa.bits-pilani.ac.in (S.C.), sumitpramanik@csmcir.res.in (S.K.P.)

<https://doi.org/10.1016/j.isci.2022.104062>



GQDs derived from neem root extract exhibit excellent cellular internalization with minimal cell toxicity (Singh et al., 2019). Neem plant extracts are also known to be a rich source of antioxidants (Islas et al., 2020; Saleh Al-Hashemi and Hossain, 2016). A recent report suggests that the relative distribution of C and N in different plant tissue (leaf and root) is expected to vary, and extracts of several parts of neem plants are a rich source of antioxidants (Tang et al., 2018; Yan et al., 2019). These extracts are chemo-preventive and show very good antitumor properties. The *in vivo* administration of GQDs had no toxic effects on blood biochemistry and caused no histopathological abnormality (Patel et al., 2019). In addition, GQDs administered in human physiology via intravenous/intramuscular/subcutaneous injection are excreted efficiently and rapidly (Li et al., 2020).

Earlier studies have shown that GQDs could differ in chemical composition, electron density, and sp^2 -hybridized carbon content depending on the synthetic methodologies adopted and carbon precursor used. Such variations account for the different mechanistic pathways of the respective GQDs for ROS-scavenging activity (Chong et al., 2016; Ruiz et al., 2017). Literature reports also reveal that the presence of a relatively higher distribution of sp^2 hybrid carbon domains, hydrogen donor functionality, and unpaired electrons caused by defects and vacancies are some of the important factors that contribute to the antioxidant activity of GQDs (Chong et al., 2016; Wang et al., 2014; Yoo et al., 2009; Zheng et al., 2015).

To date, there have been several reports that reveal that aqueous extract of neem bark and neem leaf successfully blocks ROS-induced gastric lesions in rats (Saleem et al., 2018). Bandyopadhyay et al. had reported that more than 90% of the rats treated with neem bark extract showed no evidence of gastric lesions and mucosa. These rats appeared as healthy as that of the control (Bandyopadhyay et al., 2002). It was also observed that the neem bark extract effectively inhibited pylorus-ligation-induced gastric damage in rats (85% inhibition at 20 mg/kg dose) and histamine-induced gastric lesions in guinea pigs (80% inhibition at 40 mg/kg dose) (Bandyopadhyay et al., 2002), thereby utilizing the neem bark extract as the precursor for GQDs; presumably, one can combine the advantages of both the neem bark extract and GQDs, which could be meaningful for the development of nano-antioxidants for gastric lesions. In this work, we report the synthesis of GQDs from neem bark extract following a hydrothermal procedure. Efficacy of these GQDs in scavenging intracellular ROS and anti-inflammatory effects were examined in the model of stress-induced gastric ulcer by maintaining tissue integrity. These GQDs could scavenge $\cdot OH$, $\cdot O_2^-$ and 1,1-diphenyl-2-picrylhydrazyl (DPPH \cdot), and the half-maximal effective concentration (EC_{50}) of GQDs against these three radicals were evaluated as 0.21, 0.24, and 0.19 mg/mL, respectively. GQDs are typically benign to the environment and nontoxic to human physiology (Facure et al., 2020; Tian et al., 2018). This, along with the ability of GQDs to act as a free radical scavenger, impelled us to explore the possibility of using GQDs for antioxidant therapy. Successive experiments reveal that GQD derived from Neem bark following a hydrothermal synthesis process is an efficient therapeutic candidate for ROS scavenging in the experimental swim-stress-induced gastric ulcer model. As the ROS production by macrophages is regulated via the inflammatory MMP-9-mediated pathway, evidence suggests that GQDs limit the expression of MMP-9 signaling. Therefore, these studies reveal the possibility of GQDs as a proficient scavenger for ROS and associated stress-induced gastric ulceration. This work offers a new therapeutic strategy and use of GQDs as an agent for treating gastric and intestinal dysfunctions.

RESULTS AND DISCUSSION

The GQDs were synthesized from neem bark extract following a solvothermal synthesis at 200°C temperature with a reaction time of 6 h (see details in supporting information), which were optimized based on previous works (Singh et al., 2019). Following centrifugation at 10k rpm for 10 min, the GQDs in the supernatant were isolated and purified by dialysis against deionized water for 12 h. Deionized water used for dialysis was periodically replaced after every hour. The pH of the resultant solution of GQDs was found to be 7.9 ± 0.1 ($n = 3$).

The transmission electron microscopic (TEM) images (Figure 1A) reveal that GQDs are nearly monodisperse, having average particle sizes of 5 ± 1 nm (Figure 1C). The high-resolution TEM image (Figure 1A, inset) reveals an identical well-resolved lattice fringe with a spacing of 0.30 nm, which is characteristic of the (100) in-plane lattice of graphene (Ding et al., 2016). As shown by AFM images (Figure S1A), the height of the GQDs are in the range of 4–6 nm, which indicates that the synthesized GQDs consist of 6–9 graphene layers. From TEM images, we calculated that the aspect ratio (ratio of length-to-width) of GQDs is 1–1.05, which confirms spherical morphology. The Raman spectra of GQDs show a D band at 1353 cm^{-1} and a G

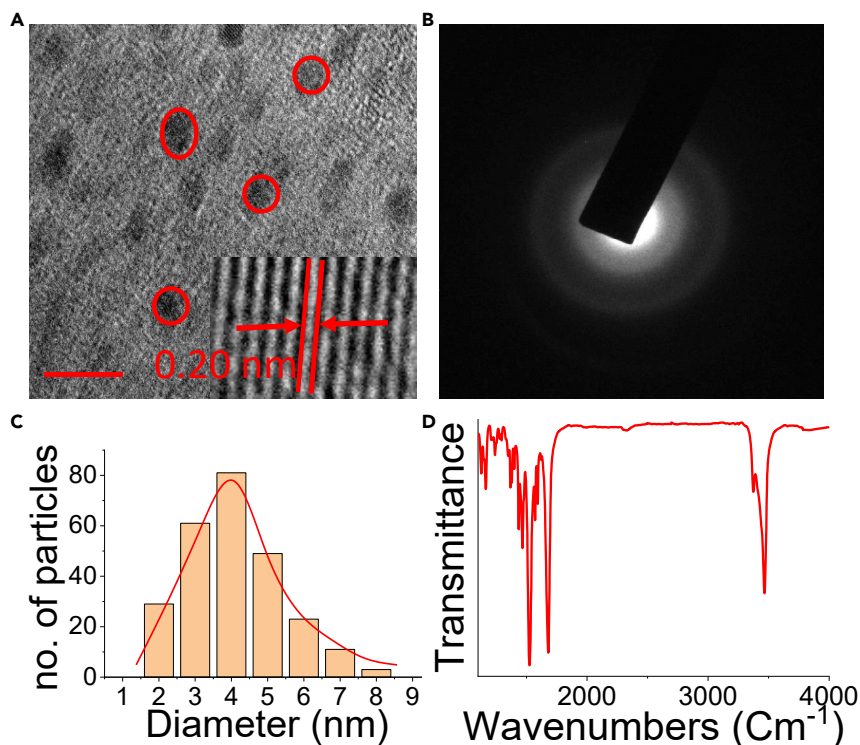


Figure 1. Morphological characterizations of GQDs

(A–D) (A) TEM image of the GQDs, in the inset HRTEM image of the GQDs; (B) FFT or SAED pattern of the GQDs; (C) size distribution of the GQDs; (D) FT-IR spectra of the GQDs. Scale bar: 6 nm.

band at 1596 cm^{-1} with a I_D/I_G intensity ratio of 0.89, which is higher than the I_D/I_G ratio of graphite powder (0.255) (Figure S1B). This indicates that the GQDs have more disordered structure than the constituent graphite powder, and this could also be due to the presence of more oxygen- and nitrogen-containing functional groups in the prepared (Li et al., 2012). Moreover, the DLS studies (in triplicate) with freshly sonicated GQD-dispersion reveal a hydrodynamic diameter of $\sim 7 \pm 2\text{ nm}$. The powder X-ray diffraction (pXRD) patterns of the GQDs show a broad diffraction peak at $2\theta = 23.9^\circ$ of the (002) plane with the “d” spacing of 0.29 nm (Figure S2). This indicates that the formed GQDs consist of very few layers of graphene sheets. In addition, the increased interlayer spacing value could be attributed to the intercalation of base between the graphene sheets and further insertion of oxygen-containing functional groups, which is consistent with previous reports on GQDs.

The Fourier transform infrared spectrum (FT-IR) of GQDs reveals a significant distribution of hydrophilic functionalities, such as O–H (3450 cm^{-1}), N–H (3230 cm^{-1}), C–O (1251 cm^{-1}), and COOH (175 cm^{-1}) on their surfaces (Figure 1D) (Ding et al., 2016); this also attributes to its good water solubility. Furthermore, the stretching vibrations of C–N= (1420 cm^{-1}), C=C (1521 cm^{-1}), and C=N (1640 cm^{-1}) bonds confirm the creation of polyaromatic structures in the GQDs during the hydrothermal reaction (Wang et al., 2012; Zhou et al., 2013).

The X-ray photoelectron spectroscopic (XPS) measurements were performed to examine the surface functionalities of the GQDs. The full spectrum is presented in Figure S3, and this shows three characteristic peaks: C 1s (285 eV), N 1s (400 eV), and O 1s (531 eV); this confirms the presence of these elements in the GQDs (Singh et al., 2019). For the high-resolution XPS spectra (Figure 2), the C 1s band can be deconvoluted into four peaks that correspond to sp^2 carbons (C=C, 284.5 eV), sp^3 carbons (C–O/C–N, 286.1 eV), carbonyl carbons (C=O, 288.5 eV), and carboxyl carbons (COOH, 290.8 eV) (Figure 2A) (Ding et al., 2016). The N 1s band can be deconvoluted into three peaks at 400.1, 401.7, and 403.3 eV, which represent pyrrolic N, Graphitic N, and amino N, respectively (Figure 2B). The O 1s band is deconvoluted into three peaks at 531.6, 532.8, and 533.5 eV for C=O, C–O, and carboxylate hydroxyl oxygen, respectively (Ding et al., 2016; Singh et al., 2019). In addition, XPS spectra suggest the distribution of the three elements present

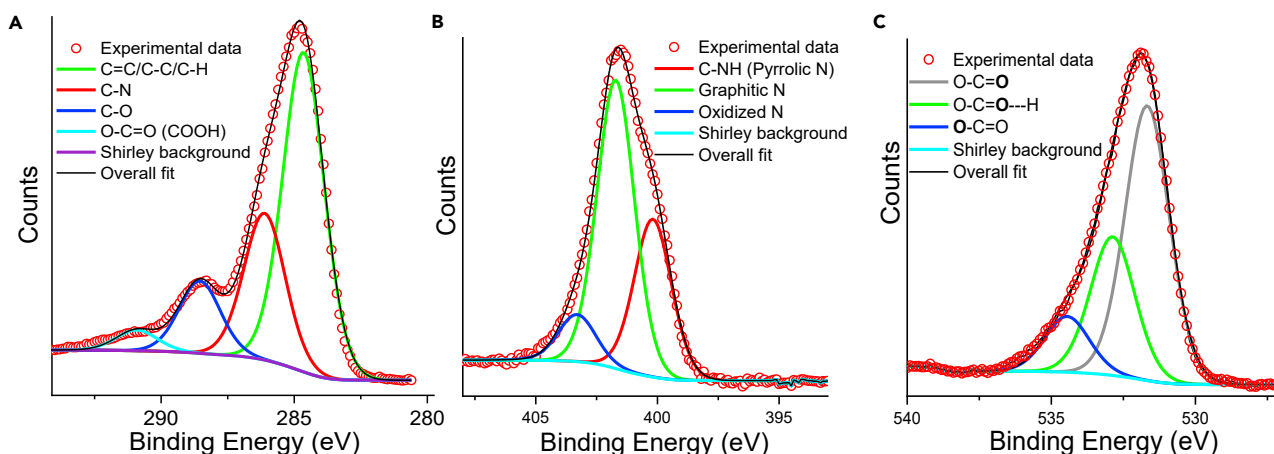


Figure 2. XPS analysis of GQDs

(A–C) High-resolution X-ray photoelectron spectra for (A) C 1s, (B) N 1s, and (C) O 1s of GQDs.

in GQDs: C = 70.2%, N = 10.8%, and O = 19.0%; this indicates that the prepared GQDs are rich in oxygen-containing functional groups (Table 1). The aforementioned data, including the AFM, pXRD, Raman, FT-IR, and XPS analysis, confirm that GQDs used for the present study are composed of π -conjugated areas in their carbon cores, whereas hydroxyl, carboxyl and amine functionalities are present on their surfaces.

The UV-Vis absorption spectrum of the as-synthesized GQDs shows an absorption band around 275 nm, which is attributed to the $\pi \rightarrow \pi^*$ transitions of the conjugated C=C bonds, whereas a broad shoulder at 295–455 nm is ascribed to the $n \rightarrow \pi^*$ transitions associated with C=N and C=O bonds (Figure 3A) (Ding et al., 2016). The GQDs also exhibit a characteristic excitation-dependent photoluminescence behavior (Singh et al., 2019). As shown in Figures 3B, 3A gradual shift in the emission maximum from 490 to 610 nm is observed with an associated shift in the respective excitation wavelength from 400 to 440 nm. It should be noted that the excitation of GQDs at 420 nm results in an optimal emission having a maximum at 550 nm. The wavelength-dependent emission properties of GQDs could be attributed to the formation of various sizes of polycyclic aromatic bunches, edge defects, surface emissive traps as well as the different size distribution of GQDs (Singh et al., 2019). The absolute fluorescence quantum yield of these GQDs is evaluated as 51%. To our knowledge, this quantum yield value compares well with that of the most reported as-synthesized GQDs derived from biomass-based feedstock and GQDs without any surface treatments.

Earlier reports suggest that the presence of the unpaired electrons and surface defects of GQDs attribute to the scavenging of the free radicals (Wang et al., 2020). The efficiency of the *in vitro* radical-quenching capability of the GQDs is evaluated by examining the scavenging activity against ROS species such as DPPH \cdot , \cdot OH, and \cdot O $^{2-}$. DPPH assay is a commonly used methodology for *in vitro* assessing of total

Table 1. XPS analysis of GQDs

Fine spectra	Energy (eV)	Species	At%
C1s	284.5	C=C, C-C, C-H	57.15
	286.1	C-N	26.34
	288.5	C-O	12.87
	290.8	O-C=O (COOH)	3.64
N1s	400.1	C-NH (Pyrrolic N)	31.93
	401.7	Graphitic N	58.33
	403.3	Oxidized N	9.74
O1s	531.6	O-C=O	58.56
	532.8	O-C-O...H	29.56
	533.5	O-C=O	11.88

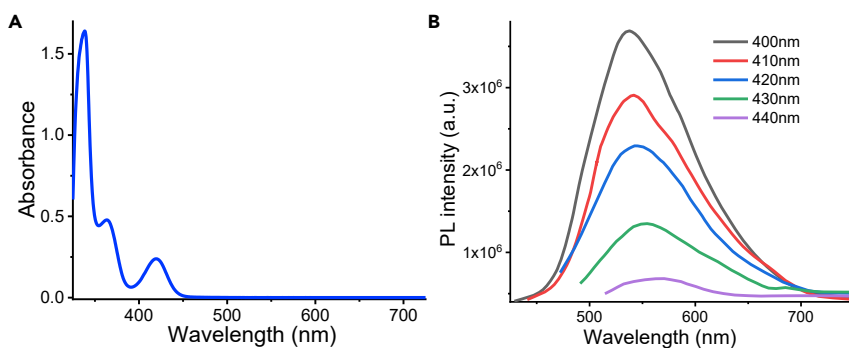


Figure 3. Optical performance of GQDs

(A and B) (A) Absorption spectrum and (B) photo illumination emission spectra of the aqueous solution of GQDs under excitation with light of different wavelengths.

antioxidant activity. GQDs show a dose-dependent scavenging effect on DPPH[•]; a steady decrease in the effective concentration of DPPH[•] with an associated decrease in the intensity of the electronic spectral band is observed with the increase of GQDs concentration (Figure S4). Moreover, the EC₅₀ of GQDs toward DPPH[•] is evaluated as 0.19 mg/mL, and this suggests that GQDs at 0.55 mg/mL can eliminate approximately 95% DPPH[•] (Figure S4). The scavenging efficiency of GQDs against DPPH[•] is possibly ascribed to the plentiful reductive functional groups on the surface of GQDs after the hydrothermal reaction. The scavenging action of GQDs toward [•]OH and [•]O₂⁻ was checked using Fenton-reaction-based assay (the detailed experimental procedure in supporting information). As shown in Figures 4A and 4B, GQDs can effectively eliminate [•]OH and [•]O₂⁻ in a dose-dependent manner. The GQDs effectively eliminate the [•]O₂⁻ and [•]OH with respective EC₅₀ value of 0.21 mg/mL and 0.25 mg/mL (Figures 4C and 4D). This dose-dependent decrease in the signal intensity and the effective concentration of [•]OH or [•]O₂⁻ radical, evaluated using Fenton-reaction-based assay, confirms the efficient scavenging of these ROS species by GQDs.

To test the potential of these GQDs for biomedical applications, biocompatibility studies using MTT assay are performed with GQDs (see Figure S5). Results of this assay indicate that the GQDs are fully biocompatible, and this makes them brilliant candidates for the therapeutic applications.

ROS, the most critical components attributed for gastric ulceration, are induced by stress that creates oxidative injury through protein oxidation and lipid peroxidation (Bhattacharyya et al., 2014; Das et al., 1997). With an aim to deal with this specific issue, we have further investigated the function of GQDs on murine-forced swim-stress-induced oxidative injury in the stomach mucosa. The ulcer index of ~70 in gastric tissues of mice was induced by swim stress for 4 h. This time point was chosen for the rest of the experiments unless mentioned otherwise. Interestingly, in this murine model of gastric ulcer, GQDs drastically reduced swim-stress-induced gastric lesions dose dependently and showed nearly 95% inhibitions at 10 mg/kg (Figure S6A). GQDs used at low (2 mg/kg b.w.) and high (10 mg/kg b.w.) doses were chosen for the rest of the experiments for the comparative analysis between low versus high dose. Microscopic examination revealed that forced swim stress caused extreme hemorrhagic wounds all through the epithelium, whereas those wounds were not found in GQDs-pretreated group, particularly at 10 mg/kg body weight (b.w) (Figure 5). Moreover, the investigation from histology of tissue indicates that the stress causes shedding of the gastric epithelial cells, besides interruption of the epithelial-mucosal barrier (red bolt) of the stomach in contrast with that of control, and the ulcer formation is prevented in tissues that are treated with varying dosages of GQDs (Figure 5A; middle and lower panel). In addition, myeloperoxidase (MPO) assay (an inflammatory marker enzyme) shows the effects of GQDs administration at a higher dose (10 mg/kg) to control/healthy mice and swim-stressed group. We did not find any toxic inflammatory activity in only GQDs-treated mice group compared with control mice (mice received only buffer solution), emphasizing safety of GQDs even at a higher dose (Table TS1). Moreover, MPO activity was significantly elevated in murine-forced swim-stress-ulcerated mucosa and that activity per gram tissue was reduced to normal level following GQDs treatment indicating the anti-inflammatory property of GQDs. Table 2 reveals the significant antioxidant activity of GQDs in protecting gastric damage. Presumably, the antioxidant activity of GQDs is induced through blockage of stress-induced augmentation in protein oxidation and lipid peroxidation. In addition, the results of the TUNEL assay (Figure 5C) indicate that stress-induced gastric cell death while pretreatment with GQDs

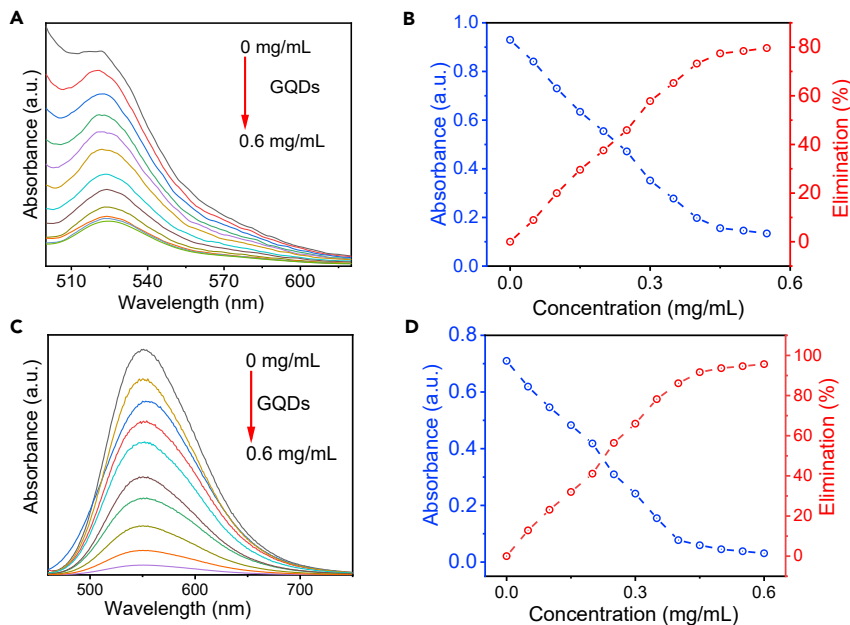


Figure 4. Demonstration of the antioxidant activity of GQDs

(A–D) (A and B) $\cdot\text{OH}$ scavenging test and (C and D) $\cdot\text{O}_2^-$ scavenging test as a function of varying the effective concentration of GQDs (0–0.6 mg/mL). Quantification of the $\cdot\text{OH}$ and $\cdot\text{O}_2^-$ radicals was achieved using a Fenton-reaction-based assay.

completely reduces that damage at a dose of 10 mg/kg b.w. Dark brown dots (Figure 5C) (black arrow) are used to indicate the end-labeling that is restricted inside the nucleus and increased DNA disintegration inside the nuclei of gastric cells after generation of forced swim stress.

Matrix metalloproteinase (MMP)-9 is well known for its inflammatory action in gastric tissues. Upon inhibition of MMP-9, pathogenesis is ameliorated; therefore, the tissues from GQDs-treated and untreated groups were processed for *in vivo* analysis of MMP-9 expression using immunofluorescence staining. Red fluorescence represents MMP-9, which is immune stained with anti-MMP-9 antibody and Texas Red conjugated secondary antibody (Figure 6A). Blue fluorescence represents DAPI-stained nuclei and documented equal fluorescence in control, stress ulcerated, and GQDs-pretreated stressed gastric tissue sections (Figure 6A). The increased expression of MMP-9 is observed in the epithelial layer and glandular regions of stress ulcerated stomach compared with control. Both low (2 mg/kg b.w.) and high (10 mg/kg b.w.) doses of GQDs-pretreated sections exhibit inhibited MMP-9 signals as evident from merging the images with corresponding DAPI-stained nuclei. Furthermore, in gelatin zymographic analysis, we found an increase in each pro and active MMP-9 activity in acute ulcerated stomach tissue extract, whereas GQDs treated at doses 2 and 10 mg/kg b.w. effectively reverse that upregulation during gastroprotection (Figure 6B). The densitometric evaluation of zymographic bands (Figure 6C) shows that stress increases the pro and active MMP-9 activity by ~60% and ~50%, respectively, in comparison with control, whereas GQDs prevent this activity and bring it almost near to control.

Furthermore, to delineate the function of GQDs in expressing secreted MMP-9, western blotting was performed using PBS extracts of control, ulcerated, and GQDs-treated tissues. Stress causes significant enhancement of MMP-9 expression in secreted form, whereas GQDs pretreatment, even at a dose of 2 mg/kg b.w, significantly reduces MMP-9 secretion during the prevention of ulceration (Figures 7A and 7B). In addition, the effect of GQDs in stress-responsive chaperone heat shock protein 70 (Hsp70) was also observed. Hsp70 expression was significantly reduced in ulcerated gastric tissue and was upregulated by GQDs (Figures 7A and 7B). The Hsps preserve cellular functional stability caused by sublethal injury and are known to induce through oxyradical, thermal, and inflammatory stress (Rafiee et al., 2006). The chaperone-denatured intracellular proteins and signal transduction proteins modulate signaling events in repetitive stress (Rafiee et al., 2006). Herein, we hypothesize GQDs-induced overexpression of anti-apoptotic

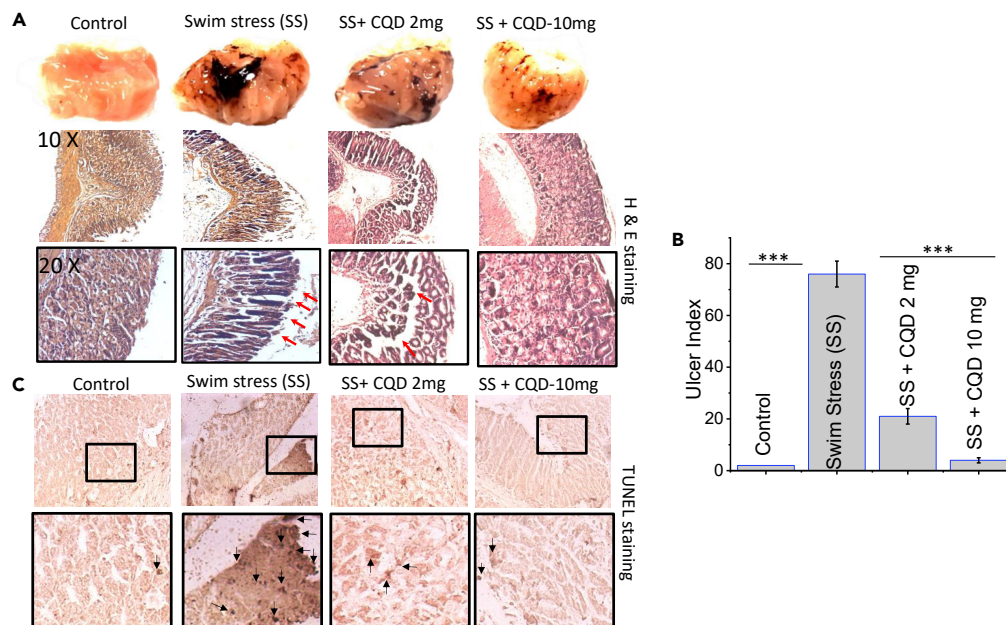


Figure 5. Protection by graphene quantum dots (GQDs) against forced swim-stress-induced gastric ulcer in mice
 (A) Macroscopic observation of control, forced swim-stressed and GQDs-treated mouse stomach (upper panel). Histological representation of gastric tissue sections from different groups. The red arrow indicates disruption of the tissue layer of the stomachs from different groups (lower panel).
 (B) Ulcer indices for each stomach and plotted for GQDs-treated and untreated groups (data were indicated as the mean \pm SEM). Evaluation between groups was executed using one-way analysis of variance (ANOVA) after that Student–Newman–Keuls t test.
 (C) TUNEL staining of gastric tissue sections from different groups. Black arrow indicates that the incidence of apoptosis was majorly concentrated in ulcerated sections.

Bcl-2 along with a sustained increased level of Hsp70 is sufficient to clear gastric damage during gastroprotection as evident from Figures 7A and 7B. However, excess and sustained accumulation of apoptotic BAX ultimately triggers BAX-dependent apoptosis and consequent caspase-3 expression (Figures 7A and 7B). Caspase-3 is one of the main initiator caspases and is linked to the mitochondrial death pathway, whereas Caspae-3 is an effector caspase (De et al., 2017). Oxidative stress damages mitochondria, which in turn results in the associated functional failure and programmed cell death. Cumulatively, GQDs significantly prevent inflammation and subsequent apoptosis in the gastric milieu even after stress by inhibiting the expression of MMP-9, BAX, and Caspase-3 and upregulating the BCL2 as evident from densitometry analysis (Figures 7A and 7B). Furthermore, to test whether GQDs could hamper the caspase signaling and lead to cell death, we have checked the caspase-9 and caspase-3 in gastric milieu by activity assay (Figure S7). The results indicate that pretreatment with GQDs significantly downregulated both caspase-9 and caspase-3 activity in a dose-dependent manner during gastroprotection (Figure S7).

Therefore, herein we report that ROS-induced MMP-9-mediated inflammation with excess mitochondrial oxidative damage and aberrant BCL2, Bax protein expressions play significant roles in swim-stress-induced gastric ulceration. Altogether, GQD acts as a double-edged sword that can promote ulcer healing via both normalizing the BCL2, Bax expression as well as by inhibition of ROS-induced MMP-9-mediated inflammation. In addition, Figure 8 shows GQDs-corrected mitochondrial dysfunction induced in swim stress. Data indicated that GQDs at 10 mg/kg prevented forced swim-stress-induced mitochondrial damage as evident from rectification of $\Delta\Psi_m$ depolarization (Figure 8A), loss of dehydrogenase activity (Figure 8B), and tissue ATP depletion (Figure 8C).

Conclusion

In brief, we report a facile method for the preparation of GQDs in water from a neem bark extract. GQDs thus produced are appropriately characterized using various analytical, spectroscopic, and electron microscopic studies. Results of the XPS studies suggest the probable distribution of hydroxyl, carboxyl, and

Table 2. *In vivo* anti-oxidative activity of graphene quantum dots (GQDs) during gastroprotection

Assays	Control	Stress	Stress + GQDs 2 mg	Stress + GQDs 10 mg
Lipid peroxidation (nmol TBARS/mg protein)	0.16 ± 0.016	0.27 ± 0.028	0.241 ± 0.024	0.20 ± 0.01
Protein carbonylation (nmol/mg protein)	1.23 ± 0.049	2.68 ± 0.15	2.15 ± 0.12	1.67 ± 0.080

Lipid peroxidation and protein carbonylation were measured as described in the materials and methods. The antioxidant activity of GQDs (10 mg/kg body weight) in protecting gastric injuries through blocking of stress-induced lipid peroxidation and protein oxidation. The results were expressed as mean ± SEM.

amine functionalities on the surfaces. GQDs are found to be an effective ROS scavenger, and the efficacy of this process is evaluated through both *in vitro* and *in vivo* studies. Results reveal a remarkable elimination efficiency, as high as 99%, against toxic ROS and effective in suppressing stress-induced gastric ulcers. To mimic the stress experienced by critically ill patients, we have adopted a model of murine-forced swim-stress-induced gastric ulcer in the laboratory. The GQDs offer gastroprotection by targeting MMP-9 pathway and reducing the inflammatory burden by suppressing excessive oxidative stress. Excess and sustained accumulations of ROS generate mitochondrial dysfunction, ultimately triggering apoptosis of gastric mucosal cells. The present study confirms the high caspase activity, overproduction of Bax, down-regulation of BCL2, and TUNEL assay. In conclusion, besides its antioxidant and anti-apoptotic properties, we could establish the mechanistic pathways for effective inhibition of inflammatory MMP-9 by GQDs that are derived from neem barks.

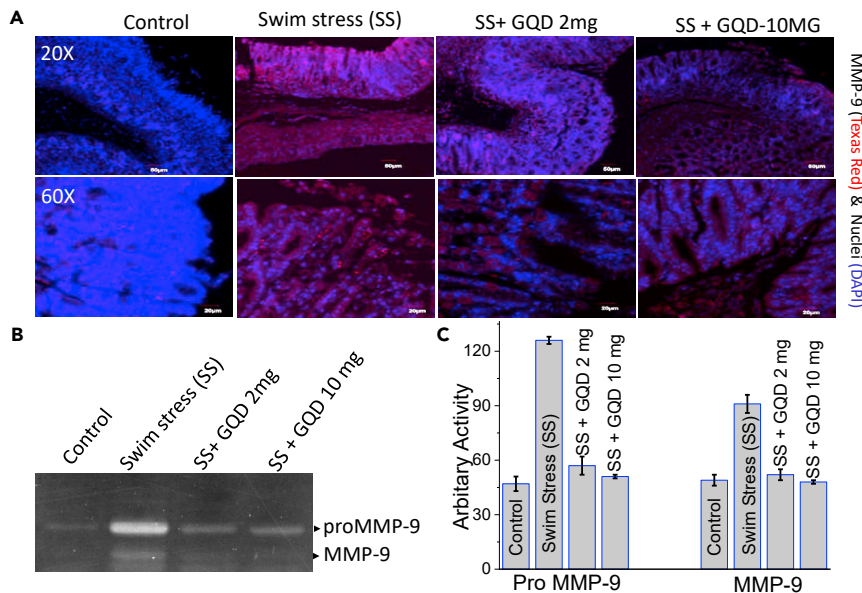


Figure 6. Gastroprotective mechanism of GQDs

(A) GQDs downregulate *in vivo* MMP-9 expression and activity in forced swim-stress-induced gastric ulcer in mice: here MMP-9 was immunostained with anti-MMP-9 antibody and Texas Red (red) conjugated secondary antibody. The nuclei were stained with 4', 6-diamidino-2-phenylindole or DAPI (blue). Both low (2 mg/kg b.w.) and high (10 mg/kg b.w.) doses of GQDs treated tissues exhibited significant inhibition of MMP-9 signals (red) compared with stress as evident from merged images with DAPI.

(B) Gelatin zymographic representation of both pro and active MMP-9 activity in acute ulcerated stomach-tissue-extract-treated, as well as GQDs-treated, groups.

(C) Histogrammic representation of pro and active MMP-9 activity in control, stress ulcerated, and GQDs-treated gastric mucosa. Graph shows fold change versus both form of MMP-9 under stress (data were indicated as the mean ± SEM). Statistical evaluation was done using ANOVA after that Student–Newman–Keuls t test.

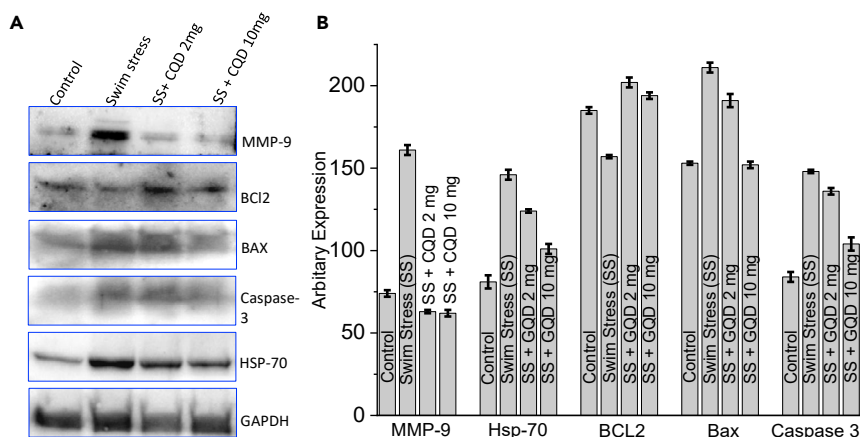


Figure 7. Anti-inflammatory and anti-apoptotic effect of QGDs during gastroprotection

(A) Effect of QGDs pretreatment (2 and 10 mg/kg b.w.) on expressions of MMP-9, BCL2, Bax, Caspase-3, Hsp70, and GAPDH (loading control) in gastric tissues after 4 h of stress as presented in respective western blots for these molecules. Each blot is representative of three independent experiments. (B) Histogrammic representation shows the significance of fold changes versus expressions of MMP-9, Hsp70, BCL2, Bax, and Caspase-3 under stress and QGDs-treated conditions compared with control (data were indicated as the mean \pm SEM). Statistical evaluation was performed using ANOVA after that Student–Newman–Keuls t test.

Limitations of the study

QGDs reported in this article are efficient in scavenging GI-ROS and preventing stress-induced gastric ulcers by targeting the MMP-9 pathway and correcting gut mitochondrial dysfunction. However, further internal validation points are necessary to evaluate the swim-stress model with additional environmental factors, including pH, temperature, and O_2 , which could impact the healing role of QGDs after ulceration caused by swim stress.

STAR★METHODS

Detailed methods are provided in the online version of this paper and include the following:

- KEY RESOURCES TABLE
- RESOURCE AVAILABILITY
 - Lead contact
 - Materials availability
 - Data and code availability
- EXPERIMENTAL MODEL AND SUBJECT DETAILS
 - Mice (Balb/c)
- METHOD DETAILS

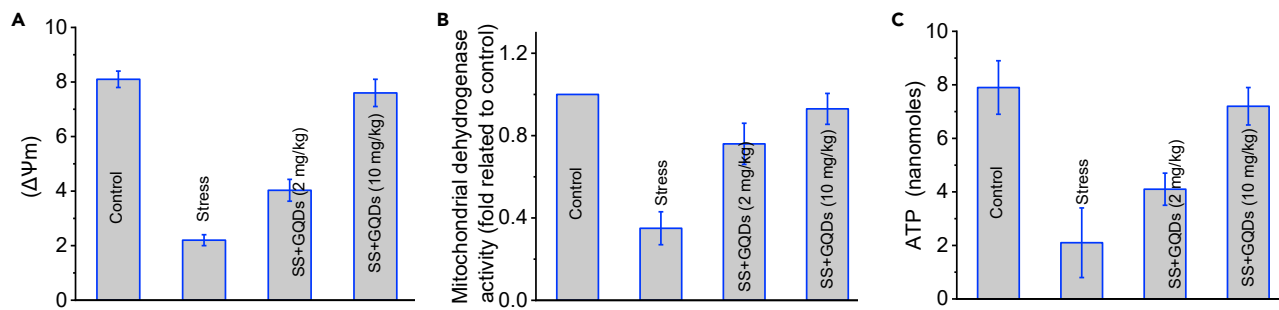


Figure 8. QGDs corrected mitochondrial dysfunction induced in swim stress

(A) Inhibition of gastric mitochondrial trans-membrane potential ($\Delta\Psi_m$) following forced swim stress was corrected by QGDs. (B) Mitochondrial dehydrogenase activity in mice gastric mitochondria after forced swim stress and protective effect of QGDs thereon. (C) Gastric mucosal tissue ATP content.

- Synthesis of QODs
- Quantum yield calculation
- Powder X-ray diffraction
- Dynamic light scattering
- Fourier transform infrared spectroscopy
- Raman spectroscopy
- Transmission electron microscopy
- DPPH[•] scavenging activity
- [•]OH scavenging activity
- [•]O₂⁻ scavenging activity
- Ethics statement for animal experiment
- Mice model of stress-induced gastric ulcer
- Histological studies and TUNEL assay
- Measurement of lipid peroxidation
- Measurement of protein carbonyl content
- Immunofluorescence
- Tissue extraction
- Gelatin zymography
- Western blotting
- Assay of Caspase-9 and Caspase-3
- Cytotoxicity study
- Measurement of gastric tissue ATP content
- Mitochondrial dehydrogenase assay
- Measurement of mucosal mitochondrial trans-membrane potential ($\Delta\psi_m$)
- Myeloperoxidase assay
- **QUANTIFICATION AND STATISTICAL ANALYSIS**

SUPPLEMENTAL INFORMATION

Supplemental information can be found online at <https://doi.org/10.1016/j.isci.2022.104062>.

ACKNOWLEDGMENTS

A.D. acknowledges SERB (India) Grants (CRG/2020/000492 & JCB/2017/000004). A.D. and S.K.P. acknowledges DBT Grant (BT/PR22251/NNT/28/1274/2017) for supporting this research. We thank Prof. Sayan Bhattacharya of IISER Kolkata for his help with the XPS analysis. This manuscript bears a CSIR-CSMCRI PRIS No: 47/2022.

AUTHOR CONTRIBUTIONS

P.C., S.B., N.K., A.C., and D.T performed the experiments; S.S., S.C., A.D., and S.K.P. supervised. All authors conceptualized, discussed, and wrote the manuscript.

DECLARATION OF INTERESTS

The authors declare no competing interests.

Received: November 5, 2021

Revised: February 15, 2022

Accepted: March 9, 2022

Published: April 15, 2022

REFERENCES

Aviello, G., and Knaus, U.G. (2017). ROS in gastrointestinal inflammation: rescue or Sabotage? *Br. J. Pharmacol.* *174*, 1704–1718. <https://doi.org/10.1111/bph.13428>.

Aviello, G., and Knaus, U.G. (2018). NADPH oxidases and ROS signaling in the gastrointestinal tract. *Mucosal Immunol.* *11*,

1011–1023. <https://doi.org/10.1038/s41385-018-0021-8>.

Bandyopadhyay, U., Biswas, K., Chatterjee, R., Bandyopadhyay, D., Chattopadhyay, I., Ganguly, C.K., Chakraborty, T., Bhattacharya, K., and Banerjee, R.K. (2002). Gastroprotective effect of Neem (*Azadirachta indica*) bark extract: possible

involvement of H⁺-K⁺-ATPase inhibition and scavenging of hydroxyl radical. *Life Sci.* *71*, 2845–2865. [https://doi.org/10.1016/S0024-3205\(02\)02143-4](https://doi.org/10.1016/S0024-3205(02)02143-4).

Bandyopadhyay, U., Das, D., Bandyopadhyay, D., Bhattacharjee, M., and Banerjee, R.K. (1999). Role of reactive oxygen species in

mercaptomethylimidazole-induced gastric acid secretion and stress-induced gastric ulceration. *Curr. Sci.* 76, 55–63.

Bhattacharyya, A., Chattopadhyay, R., Mitra, S., and Crowe, S.E. (2014). Oxidative stress: an essential factor in the pathogenesis of gastrointestinal mucosal diseases. *Physiol. Rev.* 94, 329–354. <https://doi.org/10.1152/physrev.00040.2012>.

Chong, Y., Ge, C., Fang, G., Tian, X., Ma, X., Wen, T., Wamer, W.G., Chen, C., Chai, Z., and Yin, J.-J. (2016). Crossover between anti- and pro-oxidant activities of graphene quantum dots in the absence or presence of light. *ACS Nano* 10, 8690–8699. <https://doi.org/10.1021/acsnano.6b04061>.

Das, D., Bandyopadhyay, D., Bhattacharjee, M., and Banerjee, R.K. (1997). Hydroxyl radical is the major causative factor in stress-induced gastric ulceration. *Free Radic. Biol. Med.* 23, 8–18. [https://doi.org/10.1016/S0891-5849\(96\)00547-3](https://doi.org/10.1016/S0891-5849(96)00547-3).

De, R., Mazumder, S., Sarkar, S., Debsharma, S., Siddiqui, A.A., Saha, S.J., Banerjee, C., Nag, S., Saha, D., and Bandyopadhyay, U. (2017). Acute mental stress induces mitochondrial bioenergetic crisis and hyper-fission along with aberrant mitophagy in the gut mucosa in rodent model of stress-related mucosal disease. *Free Radic. Biol. Med.* 113, 424–438.

Ding, H., Yu, S.-B., Wei, J.-S., and Xiong, H.-M. (2016). Full-color light-emitting carbon dots with a surface-state-controlled luminescence mechanism. *ACS Nano* 10, 484–491. <https://doi.org/10.1021/acsnano.5b05406>.

Facure, M.H.M., Schneider, R., Mercante, L.A., and Correa, D.S. (2020). A review on graphene quantum dots and their nanocomposites: from laboratory synthesis towards agricultural and environmental applications. *Environ. Sci.: Nano* 7, 3710–3734. <https://doi.org/10.1039/D0EN00787K>.

Islas, J.F., Acosta, E., G-Buentello, Z., Delgado-Gallegos, J.L., Moreno-Treviño, M.G., Escalante, B., and Moreno-Cuevas, J.E. (2020). An overview of Neem (*Azadirachta indica*) and its potential impact on health. *J. Funct. Foods* 74, 104171. <https://doi.org/10.1016/j.jff.2020.104171>.

Kinoshita, Y., Ishimura, N., and Ishihara, S. (2018). Advantages and disadvantages of long-term proton pump inhibitor use. *J. Neurogastroenterol Motil.* 24, 182–196. <https://doi.org/10.5056/jnm18001>.

Li, H., Yan, X., Kong, D., Jin, R., Sun, C., Du, D., Lin, Y., and Lu, G. (2020). Recent advances in carbon dots for bioimaging applications. *Nanoscale Horizons* 5, 218–234. <https://doi.org/10.1039/C9NH00476A>.

Li, Y., Zhao, Y., Cheng, H., Hu, Y., Shi, G., Dai, L., and Qu, L. (2012). Nitrogen-doped graphene quantum dots with oxygen-rich functional groups. *J. Am. Chem. Soc.* 134, 15–18.

Middha, E., and Liu, B. (2020). Nanoparticles of organic electronic materials for biomedical applications. *ACS Nano* 14, 9228–9242. <https://doi.org/10.1021/acsnano.0c02651>.

Patel, K.D., Singh, R.K., and Kim, H.-W. (2019). Carbon-based nanomaterials as an emerging platform for theranostics. *Mater. Horizons* 6, 434–469. <https://doi.org/10.1039/C8MH00966J>.

Patlevič, P., Vašková, J., Švorc, P., Vaško, L., and Švorc, P. (2016). Reactive oxygen species and antioxidant defense in human gastrointestinal diseases. *Integr. Med. Res.* 5, 250–258. <https://doi.org/10.1016/j.imr.2016.07.004>.

Pérez, S., Taléns-Visconti, R., Rius-Pérez, S., Finamor, I., and Sastre, J. (2017). Redox signaling in the gastrointestinal tract. *Free Radic. Biol. Med.* 104, 75–103. <https://doi.org/10.1016/j.freeradbiomed.2016.12.048>.

Rafiee, P., Theriot, M.E., Nelson, V.M., Heidemann, J., Kanaa, Y., Horowitz, S.A., Rogaczewski, A., Johnson, C.P., Ali, I., and Shaker, R. (2006). Human esophageal microvascular endothelial cells respond to acidic pH stress by PI3K/AKT and p38 MAPK-regulated induction of Hsp70 and Hsp27. *Am. J. Physiology-Cell Physiol.* 291, C931–C945.

Ruiz, V., Yate, L., García, I., Cabanero, G., and Grande, H.-J. (2017). Tuning the antioxidant activity of graphene quantum dots: protective nanomaterials against dye decoloration. *Carbon* 116, 366–374. <https://doi.org/10.1016/j.carbon.2017.01.090>.

Saleem, S., Muhammad, G., Hussain, M.A., and Bukhari, S.N.A. (2018). A comprehensive review of phytochemical profile, bioactives for pharmaceuticals, and pharmacological attributes of *Azadirachta indica*. *Phytotherapy Res.* 32, 1241–1272. <https://doi.org/10.1002/ptr.6076>.

Saleh Al-Hashemi, Z.S., and Hossain, M.A. (2016). Biological activities of different neem leaf crude extracts used locally in Ayurvedic medicine. *Pac. Sci. Rev. A: Nat. Sci. Eng.* 18, 128–131. <https://doi.org/10.1016/j.ppsra.2016.09.013>.

Sandler, S.E., Fellows, B., and Mefford, O.T. (2019). Best practices for characterization of magnetic nanoparticles for biomedical applications. *Anal. Chem.* 91, 14159–14169. <https://doi.org/10.1021/acs.analchem.9b03518>.

Singh, H., Sreedharan, S., Tiwari, K., Green, N.H., Smythe, C., Pramanik, S.K., Thomas, J.A., and Das, A. (2019). Two photon excitable graphene quantum dots for structured illumination microscopy and imaging applications: lysosome specificity and tissue-dependent imaging. *Chem. Commun.* 55, 521–524. <https://doi.org/10.1039/C8CC08610A>.

Strand, D.S., Kim, D., and Peura, D.A. (2017). 25 Years of proton pump inhibitors: a comprehensive review. *Gut Liver* 11, 27–37. <https://doi.org/10.5009/gnl15502>.

Tang, Z., Xu, W., Zhou, G., Bai, Y., Li, J., Tang, X., Chen, D., Liu, Q., Ma, W., Xiong, G., et al. (2018). Patterns of plant carbon, nitrogen, and phosphorus concentration in relation to productivity in China's terrestrial ecosystems. *Proc. Natl. Acad. Sci.* 115, 4033–4038. <https://doi.org/10.1073/pnas.1700295114>.

Taylor, C.T., and Colgan, S.P. (2017). Regulation of immunity and inflammation by hypoxia in immunological niches. *Nature reviews. Immunol.*

17, 774–785. <https://doi.org/10.1038/nri.2017.103>.

Tian, P., Tang, L., Teng, K.S., and Lau, S.P. (2018). Graphene quantum dots from chemistry to applications. *Mater. Today Chem.* 10, 221–258. <https://doi.org/10.1016/j.mtchem.2018.09.007>.

Ungaro, R., Mehandru, S., Allen, P.B., Peyrin-Biroulet, L., and Colombel, J.-F. (2017). Ulcerative colitis. *Lancet* 389, 1756–1770. [https://doi.org/10.1016/S0140-6736\(16\)32126-2](https://doi.org/10.1016/S0140-6736(16)32126-2).

Wang, B.B., Cheng, Q.J., Wang, L.H., Zheng, K., and Ostrikov, K. (2012). The effect of temperature on the mechanism of photoluminescence from plasma-nucleated, nitrogenated carbon nanotips. *Carbon* 50, 3561–3571. <https://doi.org/10.1016/j.carbon.2012.03.028>.

Wang, L., Li, Y., Zhao, L., Qi, Z., Gou, J., Zhang, S., and Zhang, J.Z. (2020). Recent advances in ultrathin two-dimensional materials and biomedical applications for reactive oxygen species generation and scavenging. *Nanoscale* 12, 19516–19535. <https://doi.org/10.1039/D0NR05746K>.

Wang, L., Wang, Y., Xu, T., Liao, H., Yao, C., Liu, Y., Li, Z., Chen, Z., Pan, D., Sun, L., and Wu, M. (2014). Gram-scale synthesis of single-crystalline graphene quantum dots with superior optical properties. *Nat. Commun.* 5, 5357. <https://doi.org/10.1038/ncomms6357>.

Yan, Y., Gong, J., Chen, J., Zeng, Z., Huang, W., Pu, K., Liu, J., and Chen, P. (2019). Recent advances on graphene quantum dots: from chemistry and physics to applications. *Adv. Mater.* 31, 1808283. <https://doi.org/10.1002/adma.201808283>.

Yang, Y., Zhang, M., Song, H., and Yu, C. (2020). Silica-based nanoparticles for biomedical applications: from nanocarriers to biomodulators. *Acc. Chem. Res.* 53, 1545–1556. <https://doi.org/10.1021/acs.accounts.0c00280>.

Yoo, E., Okata, T., Akita, T., Kohyama, M., Nakamura, J., and Honma, I. (2009). Enhanced electrocatalytic activity of Pt subnanoclusters on graphene nanosheet surface. *Nano Lett.* 9, 2255–2259. <https://doi.org/10.1021/nl900397t>.

Zhang, M., Bai, L., Shang, W., Xie, W., Ma, H., Fu, Y., Fang, D., Sun, H., Fan, L., Han, M., et al. (2012). Facile synthesis of water-soluble, highly fluorescent graphene quantum dots as a robust biological label for stem cells. *J. Mater. Chem.* 22, 7461–7467. <https://doi.org/10.1039/C2JM16835A>.

Zheng, X.T., Ananthanarayanan, A., Luo, K.Q., and Chen, P. (2015). Glowing graphene quantum dots and carbon dots: properties, syntheses, and biological applications. *Small* 11, 1620–1636. <https://doi.org/10.1002/sml.201402648>.

Zhou, J., Yang, Y., and Zhang, C.-y. (2013). A low-temperature solid-phase method to synthesize highly fluorescent carbon nitride dots with tunable emission. *Chem. Commun.* 49, 8605–8607. <https://doi.org/10.1039/C3CC42266F>.

STAR★METHODS

KEY RESOURCES TABLE

REAGENT or RESOURCE	SOURCE	IDENTIFIER
Gelatin	Sigma-Aldrich	CAS: 9000-70-8
Protease inhibitors cocktail	Calbiochem	Cat# 539131
Protein ladder	Puregene	Cat# PG-PMT2922
Bradford	Sigma-Aldrich	Cat# B6916
Caspase-9 assay	Calbiochem	Cat# 218824
Caspase-3 assay	Millipore	Cat# CASP3C-1kit
DAPI	Sigma-Aldrich	Cat# D9564
MMP-9	Santa Cruz	Cat# SC-6841
Bcl2	Santa Cruz	Cat# SC-492
Bax	Cell Signaling	Cat# 21125
HSP-70	Abcam	Cat# Ab- 137680
GAPDH	Santa Cruz	Cat# SC-47724
Caspase-3	Santa Cruz	Cat# SC-22140
HRP conjugated secondary	Santa Cruz	Cat# SC-2055
HRP conjugated secondary	Merck Millipore	Cat# AP-106P
HRP conjugated secondary	Santa Cruz	Cat# SC-2357
HRP Luminescent	Biorad	Cat# 1705061
Triton X-100	Sigma-Aldrich	CAS: 9036-19-5
2-4-dinitrophenyl hydrazine	Sigma-Aldrich	CAS: 119-26-6
Guanidine hydrochloride	Sigma-Aldrich	CAS: 50-01-1

RESOURCE AVAILABILITY

Lead contact

Further information and requests for resources and reagents should be directed to and will be fulfilled by the lead contact, Sumit Kumar Pramanik (sumitpramanik@csmcri.res.in).

Materials availability

This study did not generate new unique reagents.

Data and code availability

- Data: All data reported in this paper will be shared by the lead contact upon request.
- Code: This paper does not report the original code.
- Any additional information required to reanalyze the data reported in this paper is available from the lead contact upon request.

EXPERIMENTAL MODEL AND SUBJECT DETAILS

Mice (Balb/c)

Healthy Balb/c mice (20–25 g) obtained from an in-house breeding program with a “nonstress” control group (unlimited access to food and water with proper light exposure) were used for the studies. We restricted our studies to a minimum sample size, while complying with the valid statistical estimation. Ketamine (12 mg/kg b.w.) was used for anesthetizing the animals, which were then subjected to cervical dislocation. The study was discussed and approved by the ethics and animal welfare committee of the Institute of Chemical Biology (Kolkata, India), where experiments were performed.

METHOD DETAILS

Synthesis of GQDs

Neem bark extract (1 g), obtained by grinding the Neem bark into a fine powder using a commercial mixer grinder, were boiled in deionized water at 60°C for 2 h, and followed by centrifugation at 12000 g for 30 min to remove any remaining solids. The supernatant liquid solution was passed through a 0.22 μm filter membrane for further removal of any trace solid residues present in the solution. After that, this solution was used for the hydrothermal reaction. The hydrothermal reaction was performed in a stainless steel autoclave at a temperature of 200°C for 6 h. The obtained GQDs were a mixture of a transparent brown suspension along with black precipitates. The black precipitate was removed by centrifugation at 25000 g for 20 min and the supernatant was collected and washed three times with deionized water. The GQD solution was then dialyzed using a filter (cutoff 4.0 kDa) for 24 h and dried in a lyophilizer.

Quantum yield calculation

The quantum yield was calculated by using the below equation. Here both samples (GQDs) and reference were excited at a point where they have the same absorbance. Here Φ stands for quantum yield, η for refractive index, I for integrated fluorescence intensity for sample and reference.

$$\Phi_s = \Phi_{ref} \times \left(\frac{\eta_s^2}{\eta_{ref}^2} \right) \times \left(\frac{I_s}{I_{ref}} \right)$$

Powder X-ray diffraction

Powder X-ray diffraction patterns were collected in the range of 5–50° with a Philips X'pert X-ray powder diffractometer using Cu K α ($\lambda = 1.54178 \text{ \AA}$) radiation.

Dynamic light scattering

The average size and size distribution of the GQDs were measured at 27°C by DLS using Brookhaven instruments Zetapals.

Fourier transform infrared spectroscopy

The FT-IR spectroscopic measurements were carried out using a PerkinElmer GX spectrophotometer. The spectra were recorded in the range 400–4000 cm⁻¹ in KBr media.

Raman spectroscopy

Raman spectra were recorded using a Horiba LABRAM HR excited by a 514-nm laser.

Transmission electron microscopy

Transmission electron microscope images were recorded using a JEOL JEM 2100 microscope operated at 200 kV. The morphology of GQDs were obtained by placing a dilute sample on the TEM grids (lacey carbon formvar coated Cu grids (300 mesh)) using transmission electron microscopy. No additional staining was used.

DPPH[•] scavenging activity

DPPH[•], as stable nitrogen centered free radical (2,2-diphenyl-1-picrylhydrazyl), is usually used for quantitative estimation of antioxidant activity. The aqueous solution DPPH[•] is of dark purple color and has a strong absorption peak at 520 nm. The free radical scavengers pair up with the unpaired electron of DPPH[•], quenching the absorbance at 520 nm and discoloring the purple solution. The DPPH[•] solution (0.125 mmol/L) was mixed with various concentrations of GQDs and with pure HEPES buffer as the control. The absorbance intensity of this solution at 520 nm was used to evaluate the DPPH[•] scavenging efficiency. The elimination scavenging of GQDs toward DPPH[•] was calculated by using the following equation, where D_o is the absorbance at 520 nm of the control and D_s is the absorbance of the mixture of GQDs and DPPH[•].

$$\text{DPPH elimination efficiency} = (D_o - D_s)/D_o \times 100\%$$

[•]OH scavenging activity

[•]OH radicals were produced by the traditional Fenton reaction. The [•]OH radical of the Fenton reaction, reacts with salicylic acid and forms 2,3-dihydroxybenzoic acid, which has an absorption peak at 520 nm. The [•]OH scavenging efficiency of GQDs was estimated by measuring the decrease in intensity of the absorbance peak at 520 nm. Ferrrous sulfate (10.0 mmol/L), salicylic acid (10.0 mmol/L), and various concentrations of GQDs were prepared and mixed. In the control group of the experiment, the GQDs solution was replaced by HEPES buffer. After that, H₂O₂ (9.0 mmol/L) was added to the resultant solution. The [•]OH scavenging efficiency of GQDs was calculated from the below equation, where H₀ is the absorbance at 520 nm of the control and H_s is the absorbance of the mixture of GQDs and the [•]OH solution.

$$^{\bullet}\text{OH scavenging efficiency} = (H_0 - H_s)/H_0 \times 100\%$$

[•]O₂⁻ scavenging activity

The scavenging of [•]O₂⁻ was performed with a superoxide anion radical detection kit, and the principle was based on the xanthine/xanthine oxidase system. The xanthine oxidase enzyme oxidises xanthine to uric acid and [•]O₂⁻. Then the generated [•]O₂⁻ radical oxidizes hydroxylamine to nitrite, which has an absorption at 550 nm in the presence of a chromogenic agent. The [•]O₂⁻ solution was mixed with various concentrations of GQDs, and in the control group, the GQDs solution was replaced by HEPES buffer. The [•]O₂⁻ scavenging efficiency of GQDs was measured from the below equation, where S₀ is the absorbance at 550 nm of the control and S_s is the absorbance of the mixture of GQDs and the [•]O₂⁻ solution.

$$^{\bullet}\text{O}_2^- \text{ scavenging efficiency} = (S_0 - S_s/S_0) \times 100\%$$

Ethics statement for animal experiment

All animals were housed in the general animal center of the institute (CSIR-Indian Institute of Chemical Biology, Kolkata). Animal experiments were carried out following the guidelines of the Institutional Animal Ethics Committee (IAEC). Experiments were designed to minimize animal suffering and to use the minimum number associated with valid statistical evaluation.

Mice model of stress-induced gastric ulcer

Balb/c mice (20–25 g) bred in-house with free access to food and water were used for all experiments. Animals were anesthetized with ketamine (12 mg/kg b.w.) followed by cervical dislocation. Control and experimental animals were allowed to fast for 6 h with free access to water before each experiment. The ulcer was induced in Balb/c male mice by stressor using forced swim stress for 4 h at 22 ± 2°C. Carbon dots at different doses (2 and 10 mg/kg b. w.) were administered orally 1 h prior to swim stress. Next, the mice were forced to swim inside a vertical cylinder (height 40 cms and diameter 20 cms) containing water up to about 20 cms height. The height of the water column is so in tune that the mice were not able to jump out of the cylinder. Following forced swim stress, animals were sacrificed after 4 h, and the stomachs of the mice were isolated for scoring the ulcer index. Gastric lesions in the fundic mucosa are scored in a blinded manner and expressed as the ulcer index as follows: 0 for no pathology; 10 for a small pinhead ulcer, and 20–50 for lesions of 2–5 mm in length according to the standard method. The sum of the total scores divided by the number of animals indicated the mean ulcer index.

Histological studies and TUNEL assay

Gastric tissues were sectioned into 2–3 mm² pieces. The tissue samples were fixed in 4% paraformaldehyde, dehydrated, and embedded in paraffin wax. Approximately 5 μm thick serial sections were rehydrated in descending alcohol series and stained with hematoxylin and eosin or subjected to Terminal deoxynucleotidyl transferase-mediated dUTP Nick End Labeling (TUNEL) assay by using a commercial reagent kit (Millipore). Fixation, permeabilization, and staining were carried out in exact parallel to ensure comparative significance among groups. Images were captured in Olympus microscope using Camedia software (Chicago, MI, USA) and processed using Adobe Photoshop version 7.0.

Measurement of lipid peroxidation

The cytosolic fraction from the fundic stomach homogenate was used for the measurement of lipid peroxide content as thiobarbituric acid-reactive species (TBARS). Briefly, 1 mL of the cytosolic fraction was allowed to react with 2 mL of TCA-TBA-HCl (15%TCA, 0.375%TBA and 0.25N HCl) reagent, heated

in a boiling water bath for 15 min, cooled, and centrifuged. The absorbance of the supernatant was measured for nanomoles of TBARS at 535 nm ($\epsilon = 1.5 \times 10^{-5}$ M/cm).

Measurement of protein carbonyl content

Protein oxidation was measured as carbonyl content in the low-speed supernatant of the fundic stomach homogenate. The fundic stomachs from different groups of mice were homogenized in 50 mM sodium phosphate buffer, pH 7.4, in a Potter–Elvehjem glass homogenizer for 2 min to get 20% homogenate. After centrifugation at 600 g for 10 min, the proteins from 1.0 mL of the supernatant were precipitated with 10% trichloroacetic acid and allowed to react with 0.5 mL of 10 mM 2,4-dinitrophenyl hydrazine for 1 h. After precipitation with 20% trichloroacetic acid, the protein was washed thrice with a mixture of ethanol:ethyl acetate (1:1) and dissolved in 1.0 mL of a solution containing 6 M guanidine HCl in 20 mM potassium phosphate adjusted to pH 2.3 with trifluoroacetic acid followed by centrifugation. The supernatant was read for carbonyl content at 362 nm ($\epsilon = 22,000$ M/cm).

Immunofluorescence

For immunofluorescence study, the gastric tissue samples were fixed in 4% paraformaldehyde solution for 48 h, dehydrated in ascending alcohol series. It was embedded in paraffin wax and sectioned at 5 μ m thickness using a microtome. The tissue sections were deparaffinized with xylene followed by rehydration with descending alcohol series. Antigen retrieval was done by trypsin (0.05% trypsin, 0.1% CaCl_2), and blocking was performed using 5% BSA in TBS (20 mM Tris-HCl, pH 7.4 containing 150 mM NaCl) for 2 h at room temperature followed by the incubation overnight at 4°C in primary antibody solution (1:200 dilutions in TBS with 1% BSA) in a humid chamber. The tissue sections were washed four times with TBST (20 mM Tris-HCl, pH 7.4 containing 150 mM NaCl and 0.025% Triton X-100) followed by incubation with Texas red-conjugated secondary antibody (Santa Cruz Biotechnology, USA) solution (1:400 dilutions in TBS containing 1% BSA) for 2 h at room temperature. The sections were counter-stained using DAPI and images were observed in an Olympus microscope. Images at 20 \times and 60 \times magnification were captured using Camedia software (E–20P 5.0 Megapixel) and processed under Adobe Photoshop version 7.0.

Tissue extraction

The whole stomach (including fundic, body, and pyloric parts) was washed with saline and used for extraction. The stomach except for connective tissue layer (named as gastric tissue) were suspended in 10 mM phosphate buffer saline (PBS) containing protease inhibitors, minced and incubated for 10 min at 4°C. Following centrifugation at 12,000 g for 15 min, the supernatant was collected as PBS extracts. The pellet was then extracted in lysis buffer (10 mM Tris-HCl pH 8.0, 150 mM NaCl, and 1% Triton X-100 and protease inhibitors) and centrifuged at 12,000 g for 15 min to obtain TX extracts. Both PBS and TX extracts were preserved at –80°C and used in future studies. Proteins were estimated by Lowry method.

Gelatin zymography

For the assay of MMP activities, tissue extracts (70 μ g/lane) were electrophoresed in 8% SDS-polyacrylamide gel containing 1.2 mg/mL gelatin under non-reducing conditions. The gels were washed in 2.5% Triton X-100 and incubated in calcium assay buffer (40 mM Tris-HCl, pH 7.4, 0.2 M NaCl, 10 mM CaCl_2) for 18 h at 37°C and stained with 0.1% coomassie blue followed by destaining. The zones of gelatinolytic activity came as negative staining. Quantification of zymographic bands was performed using densitometry linked to proper software (ImageJ 1.52a).

Western blotting

PBS extract (100 μ g/lane) was resolved by 10% reducing SDS-polyacrylamide gel electrophoresis and processed for Western blot. Briefly, protein was transferred to membranes, blocked in 3% BSA solution in 20 mM Tris-HCl, pH 7.4 containing 150 mM NaCl and 0.02% Tween 20 (TBST) and then incubated at 4°C in 1:500 dilution of the respective primary antibodies in TBST containing 0.3% BSA. The membranes were washed with TBST, incubated with HRP conjugated secondary antibody, and bands were visualized using luminol peroxide substrate solution.

Assay of Caspase-9 and Caspase-3

The activity of Caspase-9 and -3 was measured from the gastric tissue homogenates using a commercially available kit from Calbiochem and Millipore respectively, according to the manufacturer's protocol. For

both the caspase assays equal amount of gastric tissue (20 mg) was homogenized in a specific cell lysis buffer (provided with the respective kits). The homogenate was centrifuged at $16,000 \times g$ for 15 min. The collected supernatant was quantified for protein by Bradford method and an equal amount of sample protein from different groups was used for the assays. The respective substrates for the caspases were added to the reaction mixture and incubated in the dark at 37°C for 2 h. The absorbance was taken in a spectrophotometer at 405 nm to measure the caspase activity.

Cytotoxicity study

The cytotoxicity of GQDs on human gastric epithelial cells (HGaEpC) was studied by traditional MTT assay. The cells were seeded at a density of 10^5 /well plated in 96-well plates. Cells were typically grown to 60–70% confluence, rinsed in phosphate-buffered saline (PBS), and then placed into a serum-free medium for 12 h prior to treatments. After 12 h of incubation, the cells were treated with GQDs at a concentration of 5, 10, 20, 40, 60, 80, and 100 $\mu\text{g}/\text{mL}$. After 48 h, the medium was removed, and 100 μL of fresh medium was added along with 10 μL of MTT (5 mg/mL in PBS), and incubation was continued further for 4 h at 37°C . Subsequently, MTT solution was removed, and the purple crystals were solubilized in 1.0 mL of DMSO. The absorbance was recorded at a wavelength of 550 nm in the Elisa Plate Reader. The experiment was done in triplicate.

Measurement of gastric tissue ATP content

ATP was measured with an ATP determination kit [ATP Determination Kit (A22066), Molecular Probes, Inc.] following the manufacturer's instructions. Briefly, the scraped gastric mucosa from control, swim stressed, and GQD treated stressed rats were minced, homogenized in 3% sulfosalicylic acid, and subsequently centrifuged at $12000 \times g$. The clear supernatant was used for the measurement of ATP in a luciferase-based luminometric assay. Intensity readings for the above mixtures were measured with BioTEK luminometer (at emission maximum ~ 560 nm).

Mitochondrial dehydrogenase assay

The mitochondrial metabolic function was estimated in terms of mitochondrial dehydrogenase activity. The principle of the assay was that mitochondrial dehydrogenases are capable of reducing MTT into purple-colored formazan dye, which upon dissolution in DMSO can be estimated spectrophotometrically at 570 nm. Briefly, isolated mitochondria were estimated by Lowry method, and subsequently equal amount of mitochondrial protein was incubated with MTT in PBS for 4 h at $37^{\circ}\text{C}/5\% \text{CO}_2$ condition. The samples were next centrifuged, and the precipitate was dissolved in an equal amount of anhydrous DMSO. The resultant purple-color solution was measured at 570 nm in ELISA reader (BioTek Instruments, Inc., Winooski, VT, USA).

Measurement of mucosal mitochondrial trans-membrane potential ($\Delta\psi\text{m}$)

$\Delta\psi\text{m}$ was measured as in the following way. Briefly, isolated mitochondria from stomach tissues were incubated in 500 μL of 5,5',6,6'-tetrachloro-1,1',3,3'-tetraethyl benzimidazolyl carbocyanine iodide (JC-1) assay buffer containing 300 nM of JC-1 in the darkness for 15 min. Fluorescence was measured in an F-7000 Fluorescence Spectrophotometer (Hitachi High-Technologies Corporation) (excitation, 490 nm; emission, 530 nm for JC-1 monomer, and 590 nm for JC-1 aggregates).

Myeloperoxidase assay

Myeloperoxidase (MPO) activity in the mice gastric tissues was measured by a calorimetric assay using guaiacol as the substrate. Briefly, gastric tissue homogenate prepared in 5 mM phosphate buffer was added in 1 mL of reaction buffer containing 0.5 mM H_2O_2 and 0.4 M guaiacol in 50 mM phosphate buffer, pH 7.4. The changes in the optical density per minute for tetraguaiacol were measured at 470 nm in a Shimadzu spectrophotometer. The results were expressed in units/gram gastric tissue ($\epsilon = 26.6/\text{mM}/\text{cm}$).

QUANTIFICATION AND STATISTICAL ANALYSIS

Experiments were repeated at least three times independently. The statistical analysis of the data was done using Graph Pad PRISM 5 (version 5.04) software. Comparison between groups was performed using one-way analysis of variance (ANOVA) followed by Student–Newman–Keuls T-test. Data were fitted using Graph Pad PRISM 5 (version 5.04) software represented as means \pm SEM. $p < 0.05$ was accepted as level of significance; *** very highly significant $p < 0.001$, ** highly significant $p < 0.01$; * significant $p < 0.05$; NS not significant for $p > 0.05$.